BROOKHAVEN
NATIONAL LABORATORY

BNL- 79227 -2007-CP

Electron Cloud Observations and Cures in RHIC

W. Fischer, M. Blaskiewicz, M. Brennan, H. Huang, H.-C. Hseuh, V. Ptitsyn, T. Roser, P. Thieberger, D. Trbojevic, J. Wei, S.Y. Zhang

U. Iriso, (CELLS, Bellaterra, Spain)

Presented at the ECLOUD'07 (International Workshop on Electron-Cloud Effects)
Daegu, Korea
April 9-12, 2007

June 2007

Collider-Accelerator Department

Brookhaven National Laboratory
P.O. Box 5000
Upton, NY 11973-5000
www.bnl.gov

DISCLAIMER

ELECTRON CLOUD OBSERVATIONS AND CURES IN RHIC*

W. Fischer†, M. Blaskiewicz, M. Brennan, H. Huang, H.-C. Hseuh, V. Ptitsyn, T. Roser, P. Thieberger, D. Trbojevic, J. Wei, and S.Y. Zhang, BNL, Upton, NY 11973, USA
U. Iriso, CELLS, Bellaterra, Spain

Abstract

Since 2001 RHIC has experienced electron cloud effects, which have limited the beam intensity. These include dynamic pressure rises – including pressure instabilities, tune shifts, a reduction of the stability threshold for bunches crossing the transition energy, and possibly slow emittance growth. We summarize the main observations in operation and dedicated experiments, as well as countermeasures including baking, NEG coated warm beam pipes, solenoids, bunch patterns, anti-grazing rings, pre-pumped cold beam pipes, scrubbing, and operation with long bunches.

INTRODUCTION

The Relativistic Heavy Ion Collider (RHIC), in operation since 2000, has collided species from gold ions, at energies up to 100 GeV/n, to polarized protons, at energies up to 100 GeV. Since 2001 dynamic pressure rises were observed that limited the beam intensity. At that time the cause of the dynamic pressure rise was not known. As possible causes were considered: electron impact desorption after electron cloud formation, ion-impact desorption after rest gas ionization and ion acceleration in the beam potential, and beam loss induced desorption [2]. It was later concluded that all operationally relevant pressure rises can be explained by electron clouds. Tab. 1 shows selected machine and beam parameters relevant to electron clouds for all species operated in RHIC so far.

Table 1: Main beam parameters relevant to electron clouds for all species RHIC has operated with [13].

parameter	unit	Au	Cu	d	p
atomic number Z	...	79	29	1	1
mass number A	...	197	63	2	1
revolution time $T_{\rm rev}$	μs	12.8			
rigidity, injection	Tm	81			79
rigidity, store	Tm	832			334
full bunch length, inj.	ns	15			20
full bunch length, store	ns	5			10
no. of bunches N	...	up to 111			
bunch spacing t_b	...	multiples of 108 ns			
ions per bunch N_b	10^9	1.1	50	110	200

* Work performed under US DOE contract No DE-AC02-98CH1-886.
† Wolfram.Fischer@bnl.gov

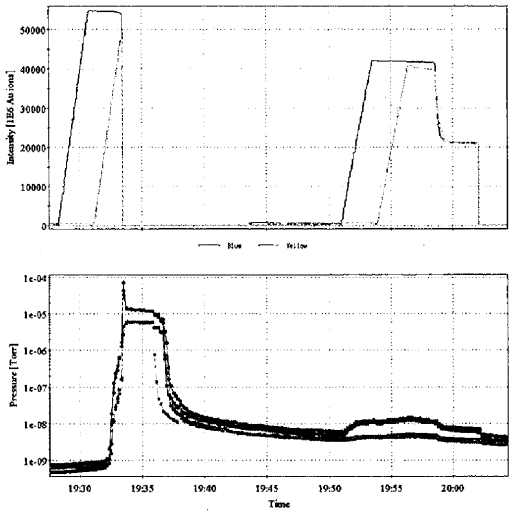

Figure 1: Blue and Yellow beam intensities (top) and pressure in an interaction region (bottom). Shown are the first two attempts to fill both rings with 110 bunches, twice the design number (October 2001) [2].

OBSERVATIONS

Observations caused by electron clouds were made during machine operation, and in dedicated experiments. The most common observation is a dynamic pressure rise caused by electron impact desorption after an electron cloud has been formed. Other observations include coherent tune shifts, direct electron observations with electron detectors, beam instabilities and beam loss, and possibly emittance growth. Although an early calculation [1] raised the possibility of an increased heat load due to electron clouds with 110 bunches, no increased heat load was observed so far.

Dynamic pressure rise

Large dynamic pressure rises were first observed in 2001 (Fig. 1) when the first attempt was made to double the number of bunches from 55 to 110. At that time the origin of the beam induced pressure rise was not known. As possible sources were considered: electron-impact desorption after an electron cloud has been formed, ion-impact desorption after rest gas ionization through the beam and subsequent acceleration of the ions in the beam potential, and ion-impact desorption after beam loss.

Dynamic pressure rise from electron-impact desorption

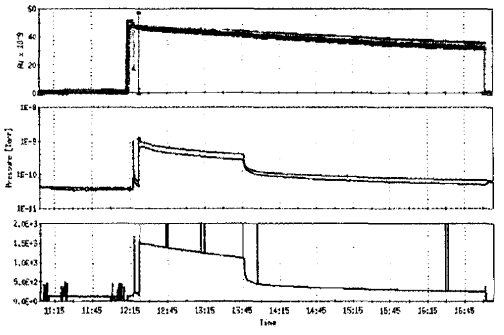

Figure 2: Pressure rise in the PHOBOS experimental area after rebucketing with 56 bunches. The beam intensity (top) slowly decays during a store, and the pressure (middle) drops sharply after some time. With high pressure the experimental background (bottom) is increased [18].

is also observed in other machines [3–6]. Ion-impact desorption after rest gas ionization lead to pressure instabilities in the ISR [7]. Ion-impact desorption is typically a problem in lower energy machines with charge-exchange processes where beam losses cannot be easily localized, like the AGS Booster [8,9], GSI SIS18 [9–11], or CERNs LEIR [12]. At the time of the first dynamic pressure rise in RHIC, ion-impact desorption coefficients for ions in the GeV/nucleon energy range were not known.

Table 2: Main parameters of the warm vacuum system.

parameter	unit	Au^{+79}	p^+
pressure p_0	Torr	$1.0 \cdot 10^{-9}$	
temperature T	K	300	
particles per bunch N_b	...	10^9	10^{11}
bunches N	...	110	
tube conductance c_{H2}	m^4s^{-1}	0.75	
tube conductance c_{CO}	m^4s^{-1}	0.25	
pumping speed S_{H2}	m^3s^{-1}	0.94	
pumping speed S_{CO}	m^3s^{-1}	0.31	
space betw. pumps $2L$	m	14	
ionization cross sec. $\sigma_{e,H2}$	m^2	$9.8 \cdot 10^{-21}$	
ionization cross sec. $\sigma_{e,CO}$	m^2	$2.2 \cdot 10^{-21}$	
ionization cross sec. $\sigma_{b,H2}$	m^2	$1.3 \cdot 10^{-19}$	$2.2 \cdot 10^{-23}$
ionization cross sec. $\sigma_{b,CO}$	m^2	$5.8 \cdot 10^{-19}$	$1.0 \cdot 10^{-22}$

To describe the pressure evolution P we consider a model that includes a static gas load Q_0, a load Q_1 from electrons in a cloud hitting the walls, a load Q_2 from rest gas molecules ionized by the cloud electrons and accelerated by the beam, a load Q_3 from rest gas molecules ionized and accelerated by the beam, and a load Q_4 from desorption after lost beam ions hit the chamber wall.

The total load is then

$$Q = Q_0 + Q_1 + Q_2 + Q_3 + Q_4 \qquad (1)$$

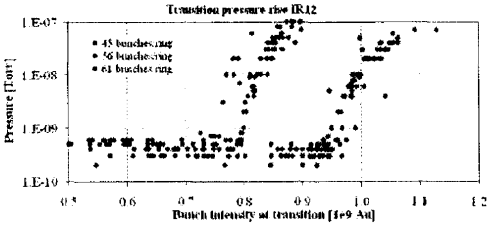

Figure 3: Transition pressure rise in IR12 with Au beams as a function of the average bunch intensity. The bunch intensity is averaged over the Blue and Yellow ring intensities, and the values before and after transition. The data is further separated into ramps with 45, 56, and 61 bunches per ring. The dots show the maximum pressure at or shortly after transition [16].

The load Q_1 per length L is

$$Q_1 = kT\frac{L}{e}\frac{dI_e}{dl}\eta_e \qquad (2)$$

where k is the Boltzmann constant, T the absolute temperature, e the elementary charge, and dI_e/dl the electron current into the wall per unit length. η_e is the average desorption coefficient for the energy distribution of the cloud electrons. The load Q_2 can be estimated as

$$Q_2 = \sigma_e P\frac{2rL}{e}\frac{dI_e}{dl}\eta_{\rm ion} \qquad (3)$$

where σ_e is the cross section for rest gas ionization from an impact of cloud electrons, r the beam pipe radius, and $\eta_{\rm ion}$ is the average desorption coefficient for ions accelerated by the beam. Values for σ_e can be found in [20]. The gas load Q_3 is [21]

$$Q_3 = \sigma_b PLN_{\rm tot}\eta_{\rm ion} \qquad (4)$$

where σ_b is the cross section for the rest gas ionization, $N_{\rm tot}$ is the beam particle flow, i.e. the number of particles in the beam divided by the revolution time. Values for σ_b can be found in Refs. [21,22]. The load Q_4 per length L is

$$Q_4 = kTL\frac{dN_{\rm tot}}{dl}\eta_{\rm ionloss} \qquad (5)$$

where $dN_{\rm tot}/dl$ is the beam intensity loss per unit length, and $\eta_{\rm ionloss}$ the average desorption coefficient for lost beam ions. $\eta_{\rm ionloss}$ is different from η_{ion} because the lost beam ions have a much higher energy than the ions generated by rest gas ionization and accelerated by the beam, and because they are lost under a grazing incidence while the ions generated by rest gas ionization are lost under close to perpendicular impact.

In equilibrium we have $PS = Q$, where S is the pumping speed. Introducing the parameter

$$b = \sigma_e\frac{2r}{e}\frac{dI_e}{dl} + \sigma_b\dot{N} \qquad (6)$$

we therefore get for the equilibrium pressure measured at the pump

$$P = \frac{Q_0 + kTL\left(\frac{1}{e}\frac{dI_e}{dl}\eta_e + \frac{dN_b}{dl}\eta_{\text{ionloss}}\right)}{S - \eta_{\text{ion}}Lb} \qquad (7)$$

Dynamic pressure rise was the first, and still is the most common electron cloud observation in RHIC [2, 14, 15]. The dynamic pressure rise could be observed with all species (p, d, Cu, Au) at injection, transition (except protons that do not cross the transition energy), and store (Figs. 1, 2, 3).

In almost all operational situations the gas load Q_1 dominates, i.e. the dynamic pressure rise is dominated by electron impact desorption after an electron cloud was formed. There are, however, a few situations where this assumption cannot explain the pressure observations. These are situations with large beam loss, the sudden pressure reduction in one of the experimental insertions, and pressure instabilities (see below).

The PHOBOS experiment (now decommissioned) had a 12 m long uncoated Beryllium beam pipe. After rebucketing, when the bunches are transferred from a $h = 360$ to a $h = 2520$ harmonic system and their length is shortened by half, an increase in the pressure by approximately one order of magnitude was observed (Fig. 2, Ref. [18]). The high pressure lead to increased and often unacceptable experimental background, and was suddenly switched off after 30 min to 2 h. The sudden switch-off very likely requires that ions are involved in the dynamic pressure rise. Without ions, the electron cloud density typically shows no second order phase transitions when the bunch intensity is changed by a small amount in simulations. Such a phase transition can be explained with the assumption of both an electron and ion cloud [19].

At transition the bunches are shortest, and the beams loose typically a few percent of their intensity when crossing the transition energy. However, the pressure rise occurs before beam loss is visible, and when sorted into bunch patterns (Fig. 3) the pressure rise is approximately proportional to the bunch intensity above a certain threshold. This feature is consistent with simulations [16].

Pressure instabilities

In some instances pressure instabilities could be observed, where the pressure growths exponentially without bounds until the beam is aborted by the beam permit system. This occurred with gold beam, in unbaked locations, and after an electron cloud was formed. Fig. 4 shows the pressure in an unbaked collimator region, which also has a geometry and materials different from most of the other warm regions. The formation of an electron cloud can be triggered after the bunch length is reduced, when, for example, bunches are transferred from the accelerating rf system into the storage rf system. From Eq. (7) a stability condition can be derived. However, in conductance limited systems a more stringent condition applies and the maximum

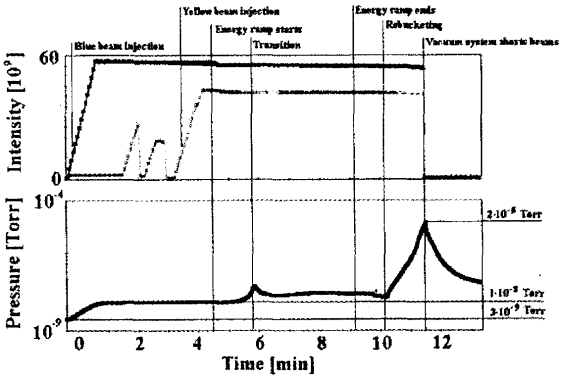

Figure 4: A vacuum instability with Au beam in the Blue ring. The upper part shows the total intensity for both rings during injection, acceleration, and storage. The lower part shows the pressure in the Blue collimator region, with an exponential increase after rebucketing [23].

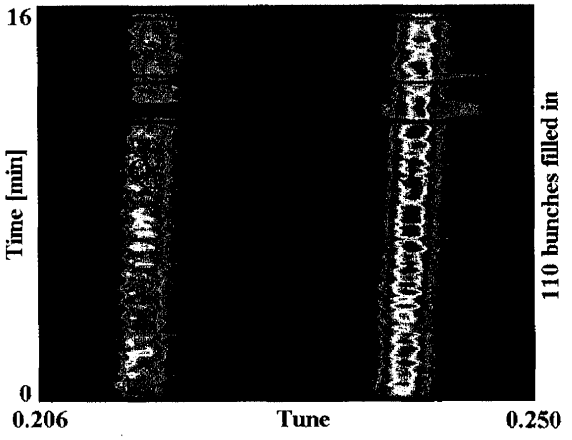

Figure 5: Coherent tunes of the last injected bunch along a train of 110 proton bunches with 105 ns spacing in the Yellow ring. Because of coupling both transverse tunes are visible [26].

desorption coefficient becomes [21]

$$\eta_{\text{crit,ion}} = \frac{\pi^2}{4}\frac{c}{bL^2}. \qquad (8)$$

An analysis shows that such an instability is possible for gases like CO [23–25].

Tune shift

After dynamic pressure rises were observed, the coherent tune shift along a bunch train was measured at injection [26]. The sign of the observed tune shift in both planes is consistent with the existence of electron clouds, and the value of the tune shift allowed a first estimate of the electron cloud density.

A bunch passing each turn through a static electron cloud with uniform spatial density ρ_e experiences a coherent tune

shift [28–30]

$$\Delta Q = \rho_e \left(\frac{r_p Z}{\gamma A}\right) \frac{\beta L}{2}. \quad (9)$$

where β is the average beta functions, assumed to be the same for the horizontal and vertical plane, L the length of the sections with electron clouds, and $r_p = 1.5347 \cdot 10^{-18}$ m the classical proton radius. With this simple model, electron cloud densities of order $\rho_e = 10^{11} - 10^{12}$ m^{-3} were estimated. The lower estimates is for the assumption of electron clouds in the whole ring, the higher estimate for the assumption of electron clouds in the warm regions only.

The estimated electron cloud densities also made possible the first comparisons with simulations [26, 27]. The simulations use the model of Ref. [31] for the secondary electron generation. Electron cloud densities of the same order of magnitude could be obtained in the simulations. The simulation results are sensitive to a number of input parameters which are not very well known [26]. The coherent tune shift due to electron clouds has not created any operational problems.

Electrons

Shortly after the first electron cloud observations were made, up to 15 electron detectors were installed in the warm regions [32, 33]. The detector design is based on a PSR design [34], although similar detectors have been installed in other machines, like APS [35], SPS [36], and BEPC [37].

With the multi-grid design (Fig. 6) it is possible to measure the cloud density, and the energy distribution of the electrons in the cloud. In Fig. 7 such a measurement is shown for a train of 43 proton bunches, 107 ns apart, with an average bunch intensity of 1.6×10^{11}. 43 bunches fill about one third of the RHIC circumference. Over the length of the bunch train the electron cloud build-up is visible. With the variable voltage on grid 1, electrons below a certain energy can be rejected, and allow a measurement of the electron energy spectrum.

For the electron-impact desorption, the electron cloud density averaged over one turn τ, the electron spectrum, and electron-impact desorption coefficient η_e is relevant. The time-averaged electron cloud density is proportional to the time-averaged voltage of the electron cloud detector

$$\langle V \rangle_\tau = \frac{1}{\tau} \int_0^\tau V(t) dt \quad (10)$$

where $V(t)$ is the instantaneous voltage signal of the electron detector. Fig. 8 shows this time-averaged electron detector signal together with a pressure reading from a vacuum gauge nearby, as Blue beam is injected. Using the same data as in Fig. 8, Fig. 9 depicts the pressure increase as a function of the average electron cloud density, which can be well fitted to a linear function. The linear fit shows

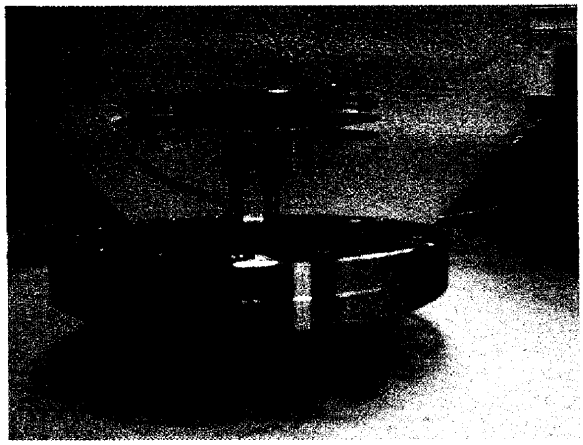

Figure 6: Multi-grid electron detector in RHIC [32].

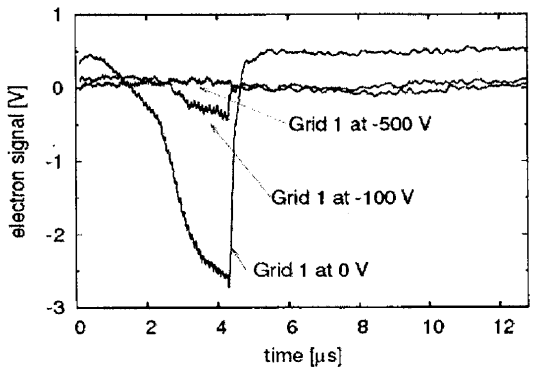

Figure 7: Electron signal of a train of 43 proton bunches, 107 ns apart, with an average bunch intensity of 1.6×10^{11}. With increasing voltage on grid 1, electrons below certain energies are rejected, allowing the measurement of electron energy spectrum in the cloud [32].

that the dynamic pressure rise is dominated by electron-impact desorption.

Fig. 10 exhibits 2 measured energy spectra. These show a large fraction of low energy electrons, with a peak around 10 eV and extending to energies of about 300 eV. The measured energy spectrum can be reproduced in simulations [38].

With measured electron cloud densities and pressure increases it is also possible to extract electron-impact desorption coefficients η_e (Fig. 11). For an unbaked stainless steel beam pipe $\eta_e = 0.01 \pm 0.005$ molecules/electron (CO equivalent) is measured, after several months of conditioning in operation. The initial value is larger by approximately a factor 5. For a baked stainless steel pipe no conditioning is visible, and the measured electron-impact desorption coefficient is $\eta_e = 0.004 \pm 0.001$ [38].

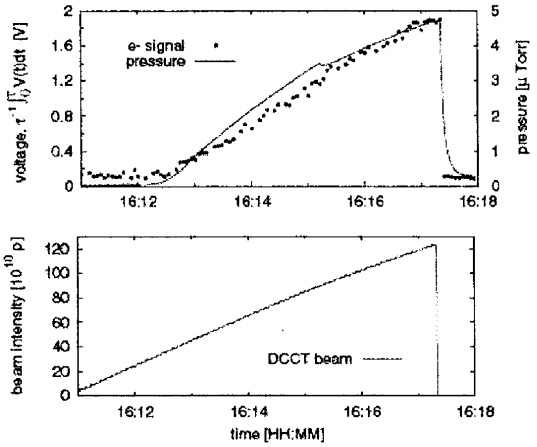

Figure 8: Pressure and electron signal evolution (top), as Blue beam is being injected (bottom) [38].

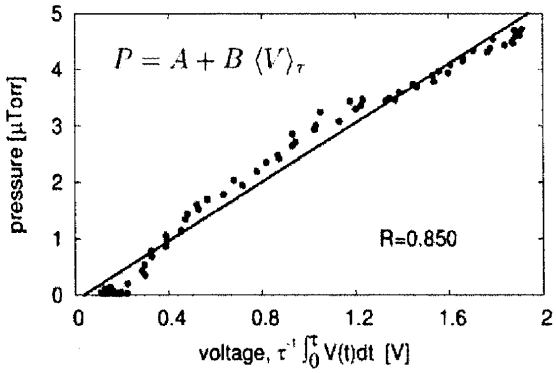

Figure 9: Pressure increase vs. average electron cloud density. Red dots are measured values, the black line is a linear fit [38].

Beam instabilities

In RHIC, the beam is most susceptible to instabilities during transition crossing. All species, except protons, cross the transition energy. Because the main magnets are superconducting, their ramp rate is slow, and transition crossing is facilitated with a γ_t-jump of fast ramping quadrupoles. Because the bunches are short, and the chromaticity across the transition energy is changed much slower than the γ_t-jump, bunches with enough intensity can become unstable. The observed instabilities are single bunch and transverse [40]. Two typical growth times were observed, 15 ms and 120 ms. In addition to a careful chromaticity setting, octupoles are used near transition to suppress instabilities. Although the instability is single bunch, it was found that electron clouds, also enhanced by the short bunch length at transition, can reduce the stability threshold. This manifests itself through increasing beam losses along the bunch train, and was observed in dedicated experiments with varying octupole and gap volt settings [41], as well as during operation in the recent Au run (Fig. 12 [42]). A review of single bunch instabilities driven by electron clouds is Ref. [43].

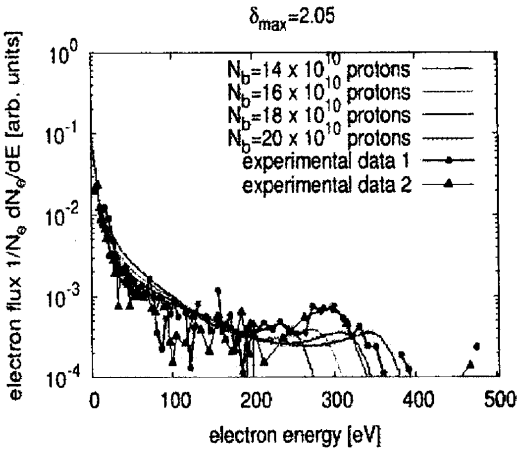

Figure 10: Energy spectrum measured, and simulated for $\delta_{\max}$ =2.05 and different bunch intensities. The spectrum shape is not significantly affected by the δ_{max}, but depends on the beam parameters (bunch intensity, length, etc.) [38].

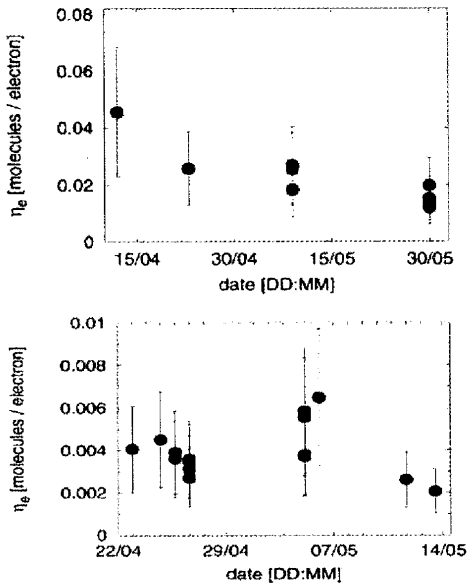

Figure 11: Calculated desorption coefficients for the unbaked stainless steel surface BO2 (top), and the baked stainless steel surface at IR12. The error bar (50%) stems from the systematic uncertainty in the pumping speed and vacuum pressure readings. A decrease of the desorption coefficient with time is noticeable for the unbaked stainless steel (top) due to the scrubbing effect [38].

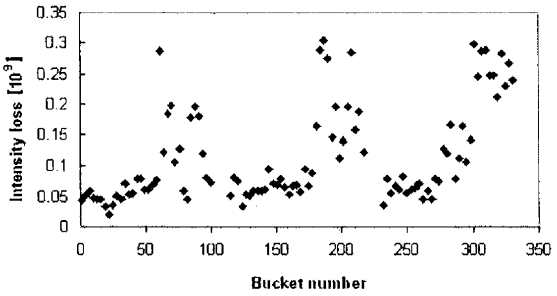

Figure 12: Yellow beam loss at transition as a function of position in the bunch train. In this pattern 8 bunches are missing after 1/3 and 2/3 of the bunch train length. The bunch train is followed by the abort gap. The intensity losses per bunch increase until a gap is reached, and then fall back because the electron cloud is reduced.

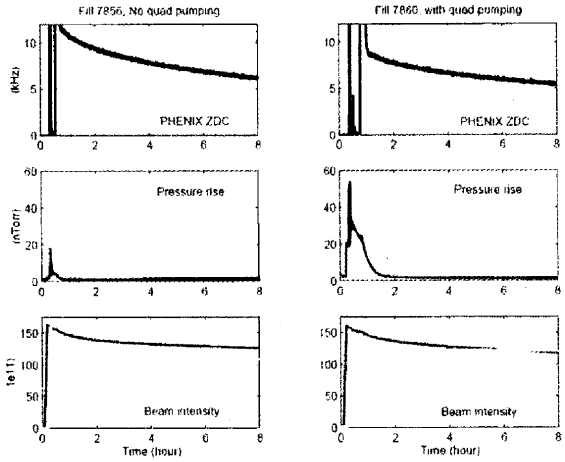

Figure 13: Event rates from collisions, sum of pressure in 4 warm locations, and beam intensity for two stores. The left column shows the standard situation, the right column shows a store for which shorter bunches were injected from the AGS [48].

Emittance growth

Incoherent emittance growth from electron clouds was investigated in Refs. [44–47], and may also be relevant to the RHIC polarized proton operation. In the most recent polarized proton run, bunches shortened through rf quadrupole pumping in the AGS were injected in order to increase the luminosity through the reduction of the hourglass effect at store. However, the luminosity of the stores with bunches of reduced length was lower than the luminosity of stores with longer bunches of comparable intensity (Fig. 13) [48,49]. At the same time, a higher dynamic pressure was observed at injection. This could be an indication that electron clouds at injection have increased the proton beam emittance. But with only a few stores with short-bunch injection, emittance growth causes other than electron clouds cannot be ruled out yet. In a separate test the emittance growth of bunches with 2×10^{11} protons at injection was measured to be 40 mm-mrad/h [15].

CURES

After the first observation of electron cloud effects a number of cures were tested, and some were implemented on a larger scale. Cures tested or implemented include in-situ baking, NEG coated warm beam pipes, solenoids, optimized bunch patterns, anti-grazing rings, pre-pumping of cold beam sections, scrubbing, and operation with longer bunches.

In-situ baking

The RHIC beam pipes in the warm regions are made of stainless steel 304L (beam pipes of the cold regions are made of 316LN). At the manufacturer the drawn tubes were detergent cleaned, water rinsed, acid prickled with $HF+HNO_3$, water rinsed again, annealed at 1050°C for 10 min, and then quenched. At BNL the pipes were cut to length, the end flanges welded. Pipes for installation in magnets were baked under vacuum at 350°C for 24 h before delivering to the magnet manufacturer.

Due to scheduling constraints, most warm beam pipes were not baked in-situ initially. After the first dynamic pressure rises were observed, a program was started to bake in-situ all warm pipes. With the exception of a few instruments, and the warm rf, this is possible at all other locations. This program yielded the first significant increase in the beam intensity.

NEG coating

Thin-film coating of beam pipes with the non-evaporable getter material TiZrV has been developed at CERN [50,51], and found large-scale applications in a number of machines including ESRF [52], RHIC [53,54], LEIR [12], and LHC [55].

The properties of typically 1 μm thick NEG coatings were measured, including activation dependent SEY, pumping speed, induced desorption, and performance deterioration due to venting cycles. After 2 h of activation at 200°C, NEG coated surfaces can reach a SEY of 1.1, and have pumping speeds of approximately 0.5 $ls^{-1}cm^{-2}$ for H_2, and initially 5 $ls^{-1}cm^{-2}$ for CO [55–58]. However, the pumping speed deteriorates with repeated venting and activation. After 10 venting/heating cycles the pumping speed is reduced by about an order of magnitude [55].

In RHIC, 55 m of NEG coated beam pipes were installed in 2003, for tests in 2004, and for comparisons with beam pipe sections that had been wrapped with solenoids. After evaluation, a decision was made to replace as much of the approximately 700 m of warm beam pipe as possible with NEG coated one. This is possible for 520 m, and until 2007 475 m were replaced (Fig. 14). The NEG coating was done

by SAES Getter [59] in Milan, Italy. Fig. 15 shows a typical NEG section bake-out and activation cycle.

The effect of the NEG coated beam pipes can be seen in Figs. 14 and 16. Fig. 16 shows that the dynamic pressure in the 12 Blue warm sections in 2004, 2005, and 2006 decreases by orders of magnitude even with increasing beam intensity. Fig. 14 shows that the total number of charges per ring increases in 2006 and 2007 together with the length of the installed NEG coated beam pipes. Note that the Au intensity in 2007 is limited by the injectors, intra-beam scattering, and instabilities at transition.

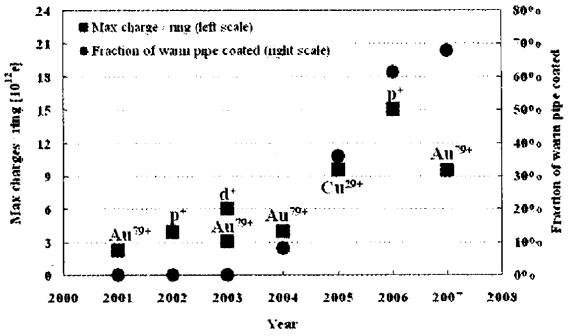

Figure 14: Total charge of RHIC beams versus fraction of warm beam pipes coated with NEG. Large-scale application of NEG pipes began in 2005. Note that the intensity of gold beams is also constraint by the injectors and intra-beam scattering, and the intensity of polarized protons by the beam-beam interaction.

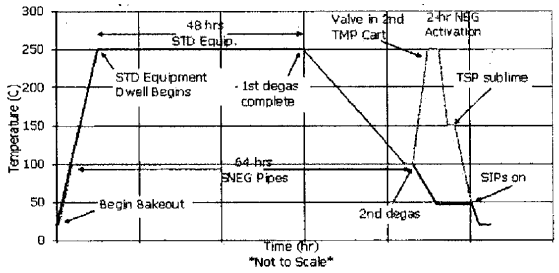

Figure 15: Typical NEG section bake-out and activation. After all surrounding components have been baked at 250°C, the NEG surface is activated.

Solenoids

In 2003 60m of solenoids were installed in the warm sections to evaluate their effect on the dynamic pressure rise. Solenoids had been successfully used in other machines to suppress electron clouds, for example in KEKB [60], PEP-II [4], and BEPC [61].

Fig. 17 shows a test of the solenoid effectiveness in suppressing the dynamic pressure rise. At a magnetic field of 1.35 mT a reduction of both the electron cloud density, and the pressure is observable. The suppression is not stronger

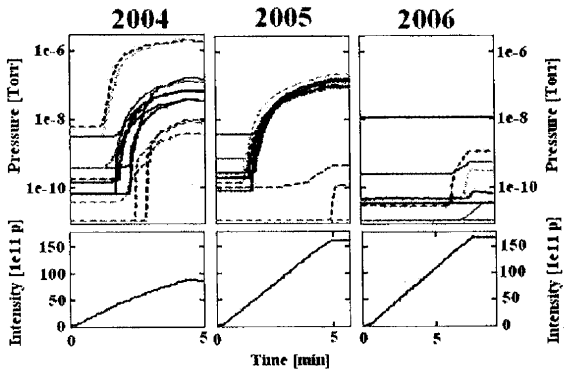

Figure 16: Dynamic pressure in 12 Blue warm straight sections (top) while proton beam with 108 ns bunch spacing is filled (bottom), in 2004-2006. The beam conditions were chosen for comparison of dynamic pressure rise, not for typical operations. With completely NEG coated pipes, the pressure in 3 sections in 2005, and 5 sections in 2006 remained at 10^{-11} Torr [54].

when the field is increased to 2.7 mT. In other tests the field has been increased up to 6 mT, but generally the dynamic pressure increase could not be suppressed completely.

A number of reasons lead to the decision to favor NEG coated beam pipes over solenoids for large scale installation in the warm areas. At comparable cost per unit length, NEG was more effective in reducing beam induced pressure increases. While both solenoids and NEG surface reduce electron clouds, only NEG surface also reduce pressure increases by other sources. With continous operation, solenoids also increase the beam pipe temperatures and lead to higher thermal outgassing. Finally, after activation, operation and m aintenance of NEG coated beam pipes is simpler and more reliable than the operation of solenoids with many small power supplies. Solenoids are still used near some experimental areas, and some equipment that cannot be baked at high temperature.

Bunch patterns

When machines are operated with less than the maximum number of bunches, the flexibility of rearranging the intensity in different bunch patterns can be used to minimize the electron cloud density, and to maximize the luminosity in a collider. With usually round beams in ion colliders the luminosity can be written as

$$\mathcal{L} = (\beta\gamma)\frac{f_0}{4\pi} N \frac{N_{\mathrm{b}1} N_{\mathrm{b}2}}{\beta^* \epsilon_N} \qquad (11)$$

where $(\beta\gamma)$ is the relativistic factor, f_0 the revolution frequency, N is the number of bunches, $N_{\mathrm{b}}1, N_{\mathrm{b}2}$ the number of ions per bunch in the two beams respectively, β^* the lattice function at the collision point (the same for the horizontal and vertical plane, and both beams), and ϵ_N the normalized rms emittance (also the same for all transverse planes).

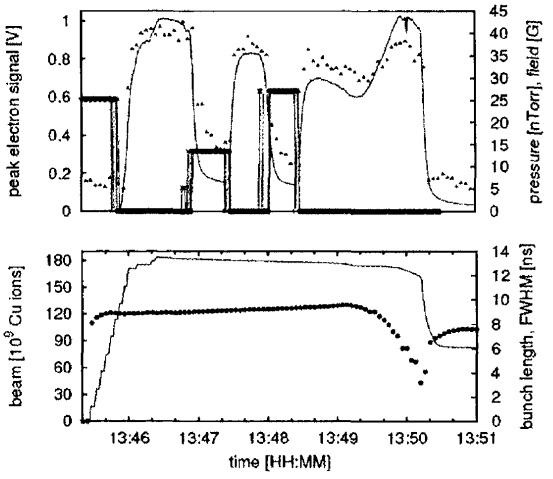

Figure 17: Effect of the solenoid field at BI12, where the entire section was covered with solenoids. Both the pressure and the electron detector signal decrease to a level for a magnetic field of 1.35 mT and 2.7 mT. At about 13:49:30, the acceleration ramp starts, the bunch length is reduced, and pressure and electron signals increase. Half of the beam is lost while crossing the transition energy (13:50:05), after which the electron cloud disappears because of the low bunch intensity [32].

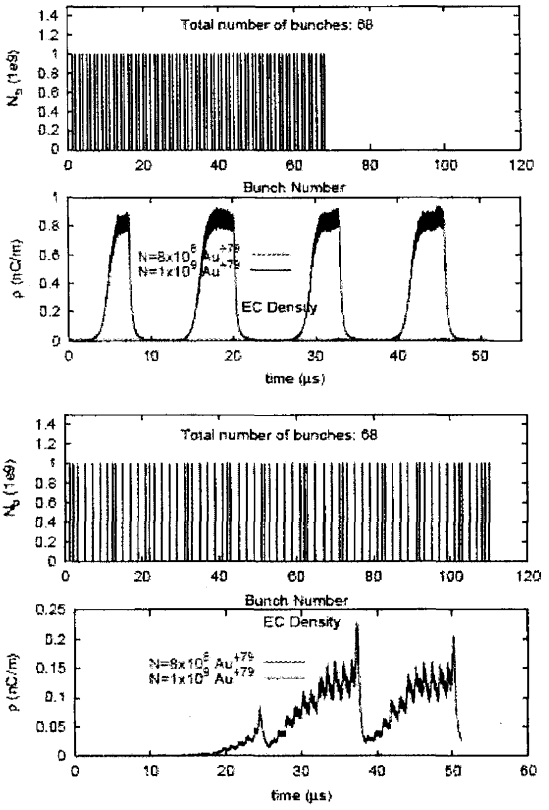

Figure 18: Simulated electron cloud evolution over 4 turns for 68 Au bunches with a single gap of maximum lengths (top), and 68 bunches distributed approximately uniformly around the circumference [62].

The same total intensity gives a higher luminosity when concentrated in fewer bunches. A simulation study and beam tests in RHIC showed that the electron cloud density is also minimized when a given total intensity is distributed in as few bunches as possible, uniformly distributed around the circumference [62]. This is shown in Fig. 18. The top plot shows the simulated electron cloud density over 4 turns for 68 Au bunches with a single gap of maximum length, the bottom shows the simulated electron cloud density for 68 Au bunches distributed approximately uniformly around the circumference. For the latter case, the peak electron cloud density is reduced by about a factor 5, the average electron cloud density even more. The problem of optimizing bunch pattern lends itself to analysis through maps for electron clouds [63].

In the RHIC run 2004 (Au-Au) the beam intensity and luminosity was limited by dynamic pressure rises in the PHOBOS experiment (Fig. 2), that lead to unacceptable experimental background [18]. During the run the number of bunches was reduced from 61 to 56 to 45 (all approximately uniformly distributed) as more bunch intensity became available from the injectors. This allowed to increase the luminosity while operating at the electron cloud limit at PHOBOS. The same limit remained in place for the 2005 Cu-Cu run. With Cu the injectors could deliver even more charge per bunch, and the number of bunches could be further reduce to 37.

Anti-grazing rings

Lost beam particles hitting the beam pipe under a grazing incident angle penetrate the beam pipe surface many times due to the surface roughness (see Fig. 19). This is expected to lead to electron and molecular desorption coefficients about two orders of magnitude higher than for perpendicular impact. In Ref. [65] a mitigation was proposed by installing anti-grazing rings, through which all particles are lost with near perpendicular impact. For a test 5 grazing rings (Fig. 20) were installed in 2 sections in RHIC, and a reduction in the dynamic pressure rise could be observed (see Fig. 21) [66].

However, for the grazing rings to be effective, they must intercept beam, which could lead to increased experimental background if they are close to a detector and beam is intercepted there which would be lost elsewhere otherwise. With the large-scale installation of NEG coated beam pipes, currently no anti-grazing rings are installed in RHIC.

Pre-pumping in cold sections

At high proton beam intensities an increase in the gas density in the cold sections was observed (Fig. 22).

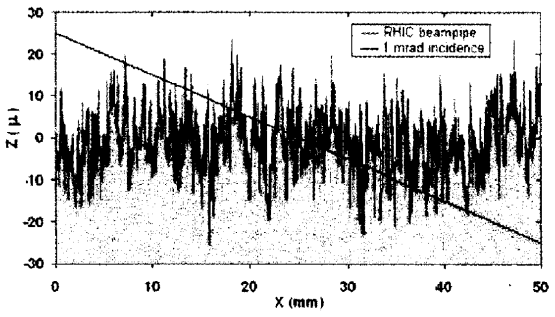

Figure 19: Single slice of a 0.2 mm × 50 mm surface scan of RHIC beam pipe material obtained by Solarius, Inc. [64] using an optical profilometer. An ion trajectory incident at 1 mrad is superimposed, showing multiple transitions between vacuum and solid [65].

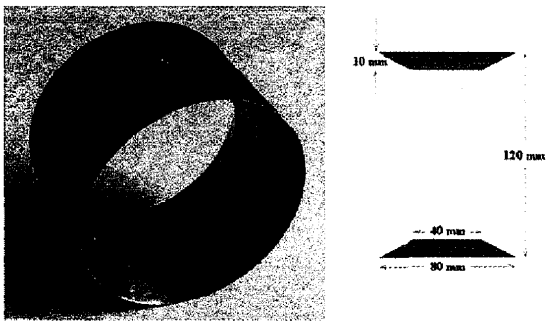

Figure 20: Photograph and cross-sectional view of one of the anti-grazing rings. In the photograph one of 5 set screws is visible. The tapering of the ridge edges is introduced to further reduced their already small impact on the ring impedance [66].

The cold sections initially relied on cryo-pumping, and had been evacuated with mobile turbo pumps to about 10^{-1} Torr only in some areas. The surface density σ of gas molecules after cool-down is

$$\sigma = \frac{pr}{2kT} \tag{12}$$

where p and T are the pressure and temperature before cool-down respectively, r the beam pipe radius, and k the Boltzmann constant. For a flat surface, a mono-layer has of order 10^{19} molecules/m^2 [67], and a pressure of 10^{-1} Torr before cool-down will result in about 5 mono-layers. Near a warm-cold transition there can be many more mono-layers.

After the observation of an increased gas density in the cold arcs, small ion pumps were installed permanently in these regions, which evacuated the beam pipe to 10^{-6} to 10^{-7} Torr before cool-down of the magnets, leading to much less than a mono-layer of gas on the cold beam pipe surface. With this no further increases in the gas density were observed.

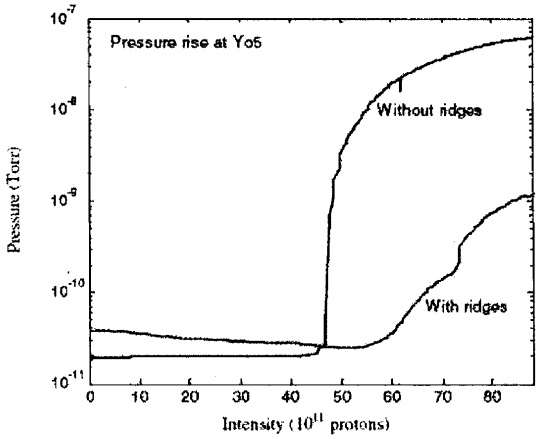

Figure 21: Dynamic pressure in warm section YO5 when 111 proton bunches with approximately 1.5 × 10^{11}protons/bunch are injected, without and with anti-grazing ridges [66].

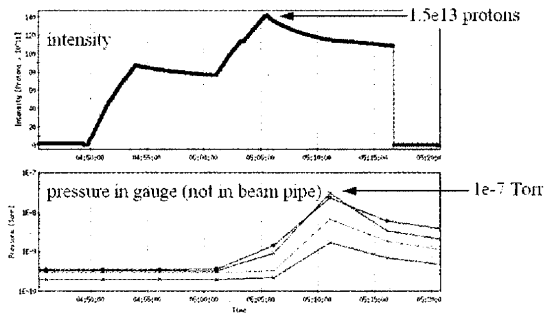

Figure 22: Increase of gas density in cold arcs (bottom) when protons are injected (top). The increase of the gas density is measured with a warm gauge connected to the cold vacuum through a small diameter conduit.

Scrubbing

Scrubbing is used routinely in the SPS [68, 69]. In RHIC scrubbing had been tested first in 2004 [70]. With scrubbing times of a few hours a reduction of the dynamic pressure rise by some 10% was observed in locations with the highest pressure. Scrubbing was most efficient in locations with large dynamic pressures.

At the beginning of the 2007 gold-gold run pressures up to 10^{-6} Torr were observed near the warm rf and a few other locations that can not be baked at high temperature. Two hours of scrubbing at injection with the highest available ion intensities, and seven fills, reduced the dynamic pressure by approximately one order of magnitude at the locations with the highest pressure (Fig. 23). Scrubbing can also be seen in the reduction of the electron-impact desorption coefficient η_e of unbaked stainless steel over the length of a run (see Fig. 11 (top)).

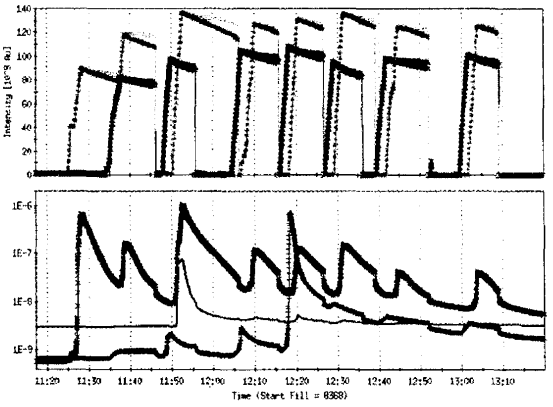

Figure 23: Scrubbing during the 2007 Au operation. Locations near the warm rf, and some instrumentation equipment cannot be baked at high temperature, and show the highest dynamic pressure. After about 2 hours of scrubbing, the dynamic pressure at these locations is reduced by more than an order of magnitude.

Operation with longer bunches

The electron cloud in RHIC in enhanced with shortened bunches. This is observable at injection, transition, and store when the bunches are shortened by a factor 2 before they are transferred into the storage rf system (see Fig. 4).

At transition, the rf voltage has been reduced from 300 kV to 150 kV to lengthen the bunches, and reduce the electron cloud density. In experiments it was observed that the intensity loss along the bunch train can be reduced in this way [41].

A small longitudinal emittance of proton beams is desirable to reduce the hour-glass effect in collision [71]. In 2006, proton stores started with an hour-glass factor of typically 0.8. Protons are injected close to and above the transition energy, where longitudinal matching is only possible when the bunches are shortened through quadrupole pumping in the AGS before transfer to RHIC. This, however, enhances the electron cloud, and may have led to incoherent emittance growth. To allow for the injection of matched bunches without an enhancement of the electron cloud density, a new rf system with harmonic number 120 is under construction (the existing acceleration system has harmonic number 360) [72]. The new cavity is common to both rings and will also ensure that the rf frequencies of the two rings are locked at all times to avoid parameter modulations from the beam-beam interaction on the ramp [73].

SUMMARY

Since 2001 electron cloud effects have limited the beam intensity in RHIC. The most common effect is dynamic pressure rises. These occurred with all species, and at injection, transition, and store. In some cases, pressure instabilities were observed. The beam intensity can also be limited because electron clouds lower the stability threshold of bunches crossing the transition energy. Recently, incoherent transverse emittance growth has been observed with protons at injection, possibly caused by electron cloud.

The main cure for electron clouds in the warm sections in RHIC are NEG coated beam pipes, which have a lower secondary electron yield than bare stainless steel pipes, and provide additional pumping. By now, almost all beam pipes that can be NEG coated have been replaced. In the cold regions, additional pumps reduced the pressure in the beam pipe before cool-down, leading to less than a mono-layer of molecules on the wall when the pipe is cold. Other cures tested, or used in limited regions, include solenoids, optimized bunch patterns, anti-grazing rings, and scrubbing.

RHIC is operating close to the dynamic pressure limit in selected warm areas that cannot be baked at high temperatures, and close to the stability threshold at transition for ions. The possible incoherent emittance growth of proton beams at injection is expected to be mitigated by a new rf system, which allows injection of longer bunches while maintaining the longitudinal emittance. If electron clouds still remain an operational problem, scrubbing would be needed to improve the machine performance.

ACKNOWLEDGMENTS

The authors are thankful for support to the members of the vacuum and accelerator physics groups. Many people from other laboratories were helpful in discussions, in particular V. Baglin, M. Furman, M. Jiménez, A. Krämer, K. Ohmi, R. Macek, E. Mahner, E. Mustafin, A. Molvik, F. Ruggiero, G. Rumolo, J.-L. Vay, and F. Zimmermann.

REFERENCES

[1] A. Drees, BNL RHIC/AP/150 (1998).

[2] W. Fischer et al., proceedings EPAC'02, Paris, France (2002).

[3] G. Arduini et al., proceedings ECLOUD'04, Napa, CA (2004).

[4] A. Kulikov, A. Novokhatski, and J. Seeman, proceedings ECLOUD'04, Napa, CA (2007).

[5] R.J. Macek et al., proceedings ECLOUD'04, Napa, CA (2004).

[6] R. Zwaska, these proceedings.

[7] O. Gröbner and R.S. Calder, PAC'73, San Francisco, CA (1973).

[8] S.Y. Zhang and L.A. Ahrens, proceedings of PAC'99, New York, NY (1999).

[9] A. Smolyakov, W. Fischer, C. Omet, and P. Spiller, GSI-Acc-Report-2005-11-001 (2005), BNL C-A/AP/117 (2006).

[10] P.J. Spiller, K. Blasche, P. Hülsmann, A. Krämer, H. Ramakers, H. Reich-Sprenger, proceedings EPAC'04, Lucern, Switzerland (2004).

[11] H. Kollmus, M.C. Bellachioma, M. Bender, A. Krämer, J. Kurdal, H. Reich-Sprenger, proceedings EPAC'06, Edinburgh, UK (2006).

[12] J. Pasternak, C. Bal, C. Carli, M. Chanel, E. Mahner, proceedings PAC'05, Knoxville, TN (2005).

[13] W. Fischer, http://www.agsrhichome.bnl.gov/RHIC/Runs/ (2007).

[14] U. Iriso et al., proceedings EPAC'04, Lucern, Switzerland (2004).

[15] S.Y. Zhang et al., proceedings PAC'05, Knoxville, TN (2005).

[16] W. Fischer and U. Iriso, BNL C-A/AP/184 (2004).

[17] S.Y. Zhang, BNL C-A/AP/198 (2005).

[18] G. Rumolo and W. Fischer, BNL C-A/AP/146 (2004).

[19] U. Iriso and S. Peggs, Phys. Rev. ST - Accel. Beams **9**, 071002 (2006).

[20] Y.-K. Kim et al., NIST physics reference data for electron-impact cross sections for ionization and excitation, http://physics.nist.gov/PhysRefData/Ionization/ (2004).

[21] O. Gröbner, in CERN 99-05, p 132 (1999).

[22] F.F. Rieke, W. Prepejchal, Phys. Rev. A **4**, p. 1507 (1972).

[23] W. Fischer, U. Iriso, and E. Mustafi n, proceedings 33rd ICFA Beam Dynamics Workshop on High Intensity and High Brightness Beams, Bensheim, Germany, AIP Conference Proceedings 773 (2004).

[24] E. Mustafi n, I. Hofmann, P. Spiller, W. Fischer, U. Iriso, P. He, H.C. Hseuh, V. Ptitsyn, S.Y. Zhang, proceedings 33rd ICFA Beam Dynamics Workshop on High Intensity and High Brightness Beams, Bensheim, Germany, AIP Conference Proceedings 773 (2004).

[25] S.Y. Zhang, BNL C-A/AP/190 (2005).

[26] W. Fischer, J.M. Brennan, M. Blaskiewicz, and T. Satogata, Phys. Rev. ST Accel. Beams 5, 124401 (2002).

[27] M. Blaskiewicz and U. Iriso, BNL C-A/AP/260 (2006).

[28] M.A. Furman and A.A. Zholents, proceedings PAC'99, New York (1999).

[29] F. Zimmermann, proceedings PAC'01 (2001).

[30] K. Ohmi, S. Heifets, and F. Zimmermann, proceedings APAC'01, Beijing; CERN SL-2001-062 (AP) (2001).

[31] M.A. Furman and M. Pivi, Phys. Rev. ST - Accel. Beams **5**, 124404 (2002).

[32] U. Iriso, Ph.D. thesis, University of Barcelona, BNL C-A/AP/228 (2006).

[33] U. Iriso et al., PAC'03, Portland, OR (2003).

[34] R. Macek et al., proceedings Workshop on Two Stream Instabilities, KEK, Tsukuba, Japan (2001).

[35] R.A. Rosenberg and K.C. Harkay, NIM A **453**, pp. 507-513 (2000).

[36] U. Iriso and J.-M. Laurent, Technical report TN03-05, LHC-VAC CERN (2003).

[37] Z.Y. Guo, proceedings PAC'01 (2001).

[38] U. Iriso and W. Fischer, Phys. Rev. ST - Accel. Beams **8**, 113201 (2005).

[39] U. Iriso and W. Fischer, Phys. Rev. ST - Accel. Beams **9**, 029901 (2005).

[40] M. Blaskiewicz et al., proceeding PAC'03, Portland, OR (2003).

[41] J. Wei et al., proceedings of the 39th ICFA Advanced Beam Dynamics Workshop on High Intensity High Brightness Hadron Beams HB2006, Tsukuba, Japan (2006).

[42] V. Ptitsyn, private communication (2007).

[43] F. Zimmermann, Phys. Rev. ST - Accel. Beams **7**, 124801 (2004).

[44] G. Rumolo, A.Z. Ghalam, T. Katsouleas, C.K. Huang, V.K. Decyk, C. Ren, W.B. Mori, F. Zimmermann, and F. Ruggiero, Phys. Rev. ST - Accel. Beams **6**, 081002 (2003).

[45] E. Benedetto, D. Schulte, F. Zimmermann, and G. Rumolo, Accel. Beams **8**, 124402 (2005).

[46] E. Benedetto, G. Franchetti, and F. Zimmermann, PRL **97**, 034801 (2006).

[47] K. Ohmi and K. Oide, Phys. Rev. ST - Accel. Beams **10**, 014401 (2007).

[48] S.Y. Zhang and V. Ptitsyn, BNL C-A/AP/257 (2006).

[49] S.Y. Zhang and V. Ptitsyn, these proceedings.

[50] C. Benvenuti et al., Vacuum **60**, pp. 57-65 (2001).

[51] C. Benvenuti et al., J. Vac. Sci. Technol. A **16** (1998).

[52] M. Hahn, R. Kersevan, I. Parat, proceedings EPAC'06, pp. 1420-1422 (2006).

[53] S.Y. Zhang, H.C. Hseuh, W. Fischer, H. Huang, T. Roser, BNL C-A/AP/220 (2005).

[54] S.Y. Zhang et al., proceedings EPAC'06 (2006).

[55] P. Chiggiato and P. Costa Pinto, Thin Film Solids **515**, pp. 382-388 (2006).

[56] A. Rossi, proceedings ECLOUD'04, Napa, CA (2004).

[57] C. Scheuerlein, B. Henrist, N. Hilleret and M. Taborelli, Applied Surface Science **172**, pp. 95-102 (2001).

[58] M. Nishiwaki and S. Kato, these proceedings.

[59] Company web site www.saesgetters.com.

[60] H. Fukuma, proceedings ECLOUD'07, Napa, CA (2007).

[61] J.Q. Wang, Z.Y. Guo, Y.D. Liu, Q. Qin, J. Xing, and Z. Zhao, proceedings ECLOUD'04, Napa, CA (2007).

[62] W. Fischer and U. Iriso, proceedings EPAC'04 (2004).

[63] U. Iriso and S. Peggs, Phys. Rev. ST - Accel. Beams **8**, 024403 (2005).

[64] Solarius Development Inc., Sunnyvale, CA, USA.

[65] P. Thieberger, W. Fischer, H.C. Hseuh, V. Ptitsyn, L.P. Snydstrup, D. Trbojevic, and S.Y. Zhang, Phys. Rev. ST - Accel. Beams **7**, 093201 (2004).

[66] S.Y. Zhang, H.C. Hseuh, P. Thieberger, D. Trbojevic, Phys. Rev. ST - Accel. Beams **8**, 123201 (2005).

[67] M. Bender, diploma thesis Fachhochschule Wiesbaden, GSI Dipl. 2003-11 (2003).

[68] J.-M. Jiménez et al., proceedings PAC'03, Portland, OR (2003).

[69] G. Arduini, T. Bohl, K. Cornelis, W. Höfle, E. Metral, and F. Zimmermann, proceedings ELOUD'04, Napa, CA (2004).

[70] S.Y. Zhang, et al., proceedings EPAC'04 (2004).

[71] M.A. Furman and M.S. Zisman, in "Handbook of accelerator physics and engineering", edited by A.W. Chao and M. Tigner, World Scientifi c (1998).

[72] M. Brennan and A. Zaltsman, private communication (2007).

[73] W. Fischer, P. Cameron, S. Peggs, and T. Satogata, BNL C-A/AP/72 (2002).